Hindawi
Shock and Vibration
Volume 2018, Article ID 1456579, 14 pages
https://doi.org/10.1155/2018/1456579

Research Article

The Maximum Height and Attenuation of Impulse Waves Generated by Subaerial Landslides

Baoliang Wang[1], **Lingkan Yao**[1,2,3], **Haixin Zhao**[1], **and Cong Zhang**[1]

[1]*School of Civil Engineering, Southwest Jiaotong University, Chengdu, Sichuan 610031, China*
[2]*MOE Key Laboratory of High-Speed Railway Engineering, Southwest Jiaotong University, Chengdu, Sichuan 610031, China*
[3]*National Engineering Laboratory for Technology of Geological Disaster Prevention in Land Transportation, Chengdu 610031, China*

Correspondence should be addressed to Lingkan Yao; yaolk@swjtu.edu.cn

Received 19 September 2017; Revised 13 December 2017; Accepted 25 December 2017; Published 24 January 2018

Academic Editor: Yuri S. Karinski

High-speed landslides that flow into reservoirs can cause impulsive water waves. To study the characteristics of the maximum impulse wave's height and its attenuation, 25 sets of flume experiments were conducted using orthogonal theory and 6 main influencing factors were considered. Taking the impulse wave heights as the evaluation criteria and analyzing the 6 influencing factors at 5 different levels, the characteristics of the maximum impulse wave's height and its attenuations were obtained. Then, statistical relationships between the maximum wave height and the controlling factors were proposed. Then, by combining the continuity equation and the hydrodynamic open channel transient flow movement equation, the process of landslide wave height attenuation was studied, and it was found that the attenuation of the wave is consistent with exponential attenuation. Then, combined with the data obtained from the orthogonal experiments, an attenuation equation for the surge was derived. Finally, the proposed equation was validated by applying it to the landslides that took place along the shore of the Zipingpu reservoir, which were triggered by the Wenchuan earthquake, and the results indicate that the calculated results are very close to the observed results.

1. Introduction

Landslides that flow into reservoirs can cause catastrophic impulse waves, threatening the safety of ships, dams, lives, and property. Several catastrophic events that resulted in a large loss of human life and property have highlighted the necessity of understanding this complex phenomenon, including the Vajont disaster, which is one of the most catastrophic phenomena ever documented involving subaerial landslide generated waves; it occurred in Italy, on 9 October, 1963. In this event, a 300×10^6 m^3 landslide flowed into the Vajont artificial reservoir and formed an 80 m high wave, which overtopped the dam, destroyed the city of Longarone, and killed 1909 people [1]. Another example of a submarine landslide related disaster is the well-documented tsunami generated by an underwater landslide triggered by a 7.0 magnitude earthquake on July 17, 1998, close to the Sissano Lagoon, Sang Dawn province, Papua New Guinea [2]. The tsunami hit an area ~30 km wide, and although the affected area was small, it caused a 15 m high run-up that killed more than 2,100 people. Many similar events have also been reported in other articles [3–6].

At present, the research on landslide waves can be divided into three categories: mathematical theories, numerical simulations, and physical models.

In terms of theoretical analysis and numerical simulation, Kennard [7] derived an expression for surface waves caused by the movement of an object in water by solving the velocity potential function of the Laplace equation. Noda [8] considered the extreme solution for landslides for the two extreme conditions of horizontal and vertical movement and deduced the analytical solution of the maximum wave height produced by these two conditions using linear approximation and infinite approximation. On the basis of Noda's work, Pan [9] proposed an equation for maximum wave by combining the results of a unidirectional flow analysis with the characteristics of the reflection and superposition of the surge. It is also found that transient waves generated

on the shore may remain trapped close to the coast due to refraction [10, 11]. Based on the Navier–Stokes equations, a two-dimensional hydrodynamic model was used to simulate the formation and propagation of waves. Pelinovsky [12] and Quecedo et al. [13] proposed a solution for the full Navier–Stokes equations, the results of which are in good agreement with real data. Ataie-Ashtiani and Malek-Mohammadi [14] simulated the surge of a rigid landslide and a flexible landslide entering the water along an inclined sliding surface using an SPH numerical simulation. Fritz et al. [15] gave a detailed analysis of landslide related surge characteristics from a two-dimensional perspective. Di Risio and Sammarco [16] proposed a new analytical solution for the leading wave based on linear theory, the result of which indicates that the wave height and period are affected by the impulse pressure and the velocity field generated during the underwater phase. By simplifying the hydrodynamic momentum equation and considering the fluid acceleration, Mulligan and Take [17] developed an equation that does not measure or estimate the length and time scale of the landslide. This equation yields the upper limit of the surge amplitude and provides a theoretical means to predict the near-field maximum water surface elevation. Yin et al. [18] employed a fluid-solid coupling model based on a general moving object collision model and the renormalization of the group turbulent model. Bosa and Petti [19] established one-dimensional and two-dimensional models for landslide surges based on the nonlinear shallow water model.

In terms of physical experiments, the triggering mechanism, that is, the landslide, can be divided into subaerial, partially submerged, and completely submerged according to the landslide's initial position [20]. Fritz et al. [21] studied the wave formation process for sliders of different sizes, shapes, and densities at varying degrees of depth along the slope. He found that the maximum wave height is related to the impact velocity, the thickness of the landslide, and the initial water depth. Noda [8] used the solid slider model to simulate the initial surge characteristics of a slider entering the water under the two extreme conditions of the horizontal and vertical movement, assuming that the initial wave height is a function of the Froude number. Heller and Hager [22] concluded through model experiments that the surge height is mainly related to the unit volume and the Froude number. Walder et al. [23] used two-dimensional physical model experiments to study the near-field characteristics of solid sliders. Their results indicate that the parameters of the near-field surge characteristics are determined by the dimensionless landslide volume per unit width, the dimensionless underwater movement time, and the dimensionless vertical impact speed. Some researchers have also studied granular landslides into lakes [24–26]. These studies suggest that the wave behavior is highly dependent on the water depth relative to the size of the landslide and that density plays a minor role in wave formation. Through three-dimensional model experiments, Frtiz et al. [27] concluded that the wave height is related to the dimensionless landslide volume, the dimensionless vertical impact speed, the dimensionless landslide thickness, and the initial water depth. In a subsequent study, by considering the energy exchange between the slider and the water, Frtiz et al. [15] concluded that the Froude number is the main factor controlling the maximum surge height. Liu et al. [28] and Enet and Grilli [29] independently conducted experiments using tanks with widths 4 times and 5.4 times larger than the landslide, respectively. These findings are very useful for near-field research but cannot be used for far-field propagation analysis because the measurements are quickly contaminated by waves reflected off of the tank's walls. Based on mixture theory, Zitti et al. [30] proposed a simple model to estimate the momentum transfer between the granular flow and the water phases. Several researchers have studied impulse waves caused by submerged landslides [10, 28, 31, 32]. The most important of these results are those of Watts [32]; that is, the formal coupling of the landslide motion to the generated waves and most of the landslide's energy are transferred to the water during an underwater landslide [33, 34]. The importance of the nondimensional time characteristic of a landslide's underwater motion, $t_s^* = t_s\sqrt{g/d}$, which can express the role of the landslide's mechanism in the process of wave generation in a simple but meaningful way, was stressed by Walder et al. [33] and Watts [31]. Through 288 sets of three-dimensional physical model experiments, Heller and Spinneken [35] also considered the underwater movement time and summarized the empirical equation for the relationship between the underwater movement time and the maximum wave height. Heller and Spinneken [35] and Heller et al. [36] directly compared 2D and 3D block models on planar hill slopes. Ataie-Ashtiani and Malek-Mohammadi [14] analyzed the wave period, height, and energy of the surge and developed an empirical equation for the period and height of the surge wave. Recently, the wave generation problem caused by a coastal tsunamigenic source, that is, a coastal mountain landslide, has been solved using experiments [37–39] in the case of both a straight coast and a circular island, and it was found that the location of the maximum run-up along the coast occurs in the near distance (about 2-3 times the width of the landslide) rather than very close to the landslide [10].

Most previous studies have considered the shape of the slider, the speed, the water depth, and other factors, but there is no specific analysis of the influence of each factor. This paper focuses on the maximum wave height of the landslide and its attenuation characteristics.

2. Model Experiments

2.1. Experimental Setup. Figure 1 shows an illustration of the flume apparatus used in this study. The flume is 9 m long, 0.5 m wide, and 0.7 m high. The two sidewalls are transparent tempered glass, so the wave propagation in the flume can be observed. A digital camera was placed near the point where the concrete block impacts the water to record the form of the landslide surges. Seven wave height gauges were arranged along the central axis of the water flume in the direction of the surge motion, and a water level hydrograph at each point was set to record after the water wave was formed. To convey solid blocks, an inclined plane with an adjustable slope (30–90°) was designed. The slope's length was 2.5 m, the slope is made of stainless steel marked with a scale, and the plane's surface was lubricated to reduce friction.

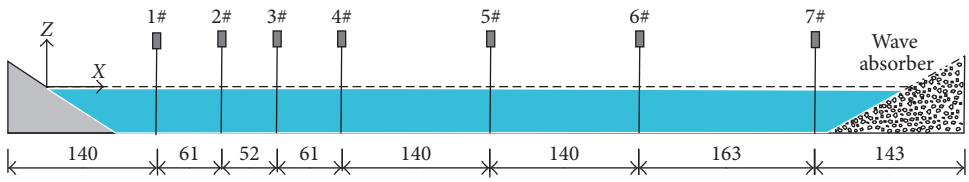

Figure 1: Schematic of the flume device.

2.2. Experimental Measurements. The blocks used were solid blocks with zero porosity, and the landslide model was designed to simulate real geometry and bulk density characteristics. The back of the landslide block has a hanger, and the hanger is attached to a string. The landslide body was placed on the surface of the inclined plane. The string was cut before sliding starts, and the landslide was free to slide on the surface under the force of gravity. The trajectory of the block was recorded by the digital camera. According to the time series pictures of the different displacements, the displacement (L) of the landslide body at time (t) was obtained. The maximum wave height was obtained from the digital camera, and the time of the underwater landslide motion (t_s) was read frame by frame from industrial camera footage.

2.3. Experimental Design. Many physical variables can affect the maximum wave height, and the wave height can be represented as a function of all of the physical parameters involved as follows:

$$A = f\left(s, w, l, v_s, d, h, w_f, t_s, \alpha, \rho_s, \rho_w, g, \mu, v, r, p\right), \quad (1)$$

where l, w, and s are the length, width, and thickness of the modeled landslide, respectively; d is the still water depth; h is the drop height of the landslide; w_f is the width of the flume; t_s is the time of the landslide's underwater motion; α is the angle of the inclined plane; ρ_s and ρ_w are the landslide and water densities, respectively; g is the gravitational acceleration; μ is the water viscosity; v is the landslide impact velocity; r is the distance from the drop point; and p is the porosity of the landslide. With the simplifications introduced by Panizzo et al. [40], the main parameters selected for this study are the sliding impact velocity (v), the slide width (w), the slide thickness (s), the slide length (l), the slide's slope (α), the still water depth (d), the drop height of the mass's center (h), and the landslide's underwater motion time (t_s).

These factors can be combined into five dimensionless factors as follows:

Slide Froude number:

$$F = \frac{v}{\sqrt{gd}}. \quad (2)$$

Dimensionless slide volume:

$$V = \frac{V_s}{wd^2}. \quad (3)$$

Blockage ratio:

$$B = \frac{w}{w_f}. \quad (4)$$

Table 1: Factors and levels of the orthogonal experiment.

Level	parameter					
	d (m)	w (m)	s (m)	l (m)	h (m)	α (°)
1	0.25	0.07	0.07	0.1	0.3	30
2	0.3	0.1	0.1	0.12	0.45	45
3	0.35	0.12	0.12	0.15	0.6	60
4	0.4	0.15	0.15	0.2	0.75	70
5	0.45	0.2	0.2	0.25	0.9	90

Nondimensional time of the landslide underwater motion:

$$T_s = t_s\sqrt{\frac{g}{d}}. \quad (5)$$

Slide impact angle:

$$\alpha_0 = \left(\frac{\alpha}{360}\right) \times 2\pi \quad \text{(in radians)}. \quad (6)$$

The experimental sets were designed using the orthogonal method, which is the most useful design method in multifactor experiments. The theory of orthogonal design is a branch in the field of mathematics and is deeply studied by several great number theorists, such as Radom and Hurwitz. The encyclopedic work of Geramita and Seberry [41] is a good reference for the orthogonal method. A classic result of this method is attributed to Radom, since he determined the dimensions in which orthogonal designs exist; more information on this method and physical discussion of how this technique was applied in this study is provided in the Appendix. The experiment sets of this study were performed at 5 levels for each factor using an $L_{25}5^6$ orthogonal table. The experimental scheme was compiled according to the orthogonal table, and 25 sets of experiments were carried out, as is shown in Table 1.

3. Experimental Results

3.1. Velocity of Slide. The block sliding process was recorded by a digital camera, which recorded 25 frames per second with a frame interval of 0.04 seconds. Thus, the location of the mass's center at different times could be obtained. The block's movement can be simplified as the movement of the slider on the inclined plane with a friction coefficient (μ). Figure 2 shows the force analysis of the slide block.

The acceleration along the inclined plane can be calculated by

$$a = g\left(\sin\alpha - \mu\cos\alpha\right). \quad (7)$$

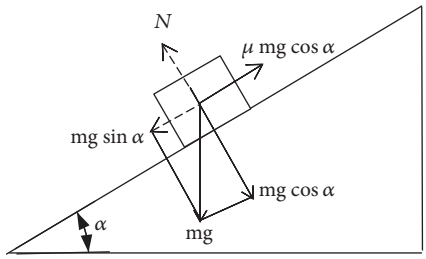

Figure 2: Forces acting on the sliding block.

The velocity can be obtained by

$$v_s = \sqrt{2as} = \sqrt{2gh\left(1 - \mu\cot\alpha\right)}, \tag{8}$$

where g is the acceleration due to gravity (9.8 m/s^2); α is the slope angle (°); h is the drop height of the mass's center (m); and μ is the friction coefficient.

Using (8), we analyzed 8 sets of experimental videos and obtained 8 friction coefficients, with an average value of 0.460 and a variance of 1.77×10^{-5}. Figure 3 shows a comparison between the calculated and measured slide velocities derived from three experiments. The measured velocities are very close to those calculated using (2); therefore, we can obtain the slide velocity using (8).

3.2. Analysis of the Importance of the Influencing Factors. In orthogonal design, due to the different experimental conditions, we cannot compare the two specific sets of experimental data. However, if the experimental results are properly combined, they can be compared. The impulse wave heights obtained under the various experimental conditions are listed in Table 2. In the following discussion, we analyze and calculate the data in the table.

3.2.1. Influence of the Different Values of the Experimental Indexes for the Same Factors. We use d_j to represent the jth level of factor d, where $j = 1, 2, 3, 4, 5$. The d_1 levels (25 cm) of the d factors were calculated, and the experimental indexes in experimental schemes 1, 2, 3, 4, and 5 were calculated for d_1. For these conditions, the cumulative height of the surge is

$$d_1 = I_1 = 21 + 33 + 42 + 51 + 68 = 215. \tag{9}$$

The average value for experimental index A_1 is as follows:

$$\overline{d_1} = \overline{I_1} = \frac{215}{5} = 43. \tag{10}$$

The average values of the experimental indexes for d_2, d_3, d_4, and d_5 are 40.8, 41.8, 41.8, and 42.8, respectively.

In the 5 experiments using d_1 (experiments (1)–(5)), b, s, l, h, and α were evaluated at 5 different levels, and each appeared 1 time. Similarly, for the 5 experiments using d_2 (experiments (6)–(10)), b, s, l, h, and α were evaluated at 5 different levels, and each appeared 1 time. By this analogy, in the d_1, d_2, d_3, d_4, and d_5 conditions of the 5 experiments, although other conditions (b, s, l, h, α) have changed, these

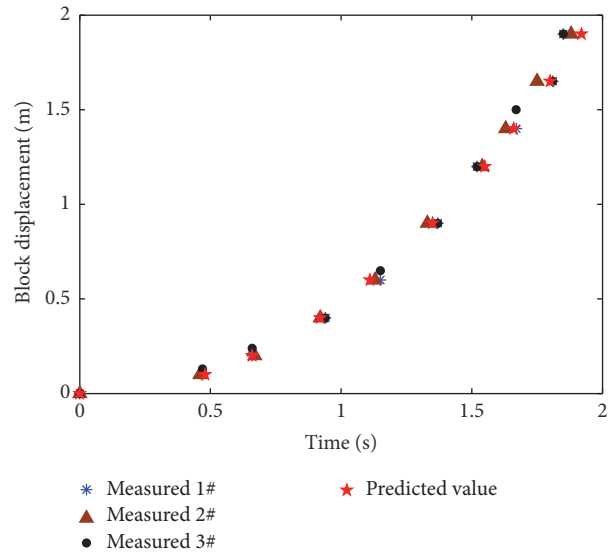

Figure 3: Comparison between the measured evaluated slide velocities and those obtained from (8).

changes are "balanced," which makes d_1 (I_i), d_2 (II_i), d_3 (III_i), d_4 (IV_i), and d_5 (V) comparable. The difference between the four factors reflects the effect of the four values of the d factor (still water depth) on the wave height. Through data comparison of different levels, it can be seen that $d_1 > d_5 > d_4 > d_3 > d_2$. d_1 has a maximum value of 215, and d_2 has a minimum value of 204, so when the d factor is at level 1, the wave height is maximized. The significance of this is that when the d factor is 25 cm, the wave height value can be increased by an average of 2.2 mm compared to the minimum value (2 level; 30 cm). Similarly, we can calculate the average value of b, s, l, h, and α for different values. The results of the experimental data are listed in Table 3. I_i, II_i, III_i, IV_i, and V_i in Table 3 represent the sum of the experimental indicators of factor i at the first, second, third, and fourth levels.

3.2.2. Range Analysis. The range is defined as the difference between the best and worst level of the factor. Range analysis is mainly used to clarify the significance levels of the different influencing factors on the wave height, and those most significant factors can be determined based on the results of the range analysis. It is important to measure the fluctuation of the data. The range of each factor in Table 4 is calculated as R_i, the range of the d factor is $R_1 = \overline{\mathrm{I}_1} - \overline{\mathrm{II}_1} = 43 - 40.8 = 2.2$. Similarly, the range of the b, s, l, h, and α factor is 4.8, 14, 8.8, 14.8, and 5, respectively. Figure 4 shows the influence of the various factors on the wave height. The abscissa is expressed by the different levels of the factors, and the ordinate is the wave height. Comparison of the graphs can clearly show the wave height at the most effective value of the factors. As can be seen from Figure 4, of the factors affecting the wave height, the range of the drop height is the largest, and it produces a large difference in the wave height; therefore, the drop height is the main influencing factor. Through range comparison and intuitive graphical analysis, it can be concluded that the sliding slope is the main factor affecting the wave height,

Table 2: Experiment schemes and results.

Experiment number	d (cm)	b (cm)	s (cm)	l (cm)	h (cm)	α (°)	Results (mm)
(1)	25	7	7	10	30	30	21
(2)	25	10	10	12	45	45	33
(3)	25	12	12	15	60	60	42
(4)	25	15	15	20	75	70	51
(5)	25	20	20	25	90	90	68
(6)	30	7	10	15	75	90	44
(7)	30	10	12	20	90	30	46
(8)	30	12	15	25	30	45	38
(9)	30	15	20	10	45	60	41
(10)	30	20	7	12	60	70	35
(11)	35	7	12	25	45	70	42
(12)	35	10	15	10	60	90	42
(13)	35	12	20	12	75	30	46
(14)	35	15	7	15	90	45	42
(15)	35	20	10	20	30	60	37
(16)	40	7	15	12	90	60	47
(17)	40	10	20	15	30	70	41
(18)	40	12	7	20	45	90	38
(19)	40	15	10	25	60	30	42
(20)	40	20	12	10	75	60	41
(21)	45	7	20	20	60	45	51
(22)	45	10	7	25	75	60	41
(23)	45	12	10	10	90	70	42
(24)	45	15	12	12	30	90	34
(25)	45	20	15	15	45	30	46

Table 3: Orthogonal analysis of experimental data.

	d	b	s	l	h	α
I_i	215	205	177	187	171	201
II_i	204	203	198	195	200	164
III_i	209	206	205	215	212	249
IV_i	209	210	224	223	223	211
V_i	214	227	247	231	245	226
$k_1 = I_1/5$	43	41	35.4	37.4	34.2	40.2
$k_2 = II_1/5$	40.8	40.6	39.6	39	40	41
$k_3 = III_1/5$	41.8	41.2	41	43	42.4	41.5
$k_4 = IV_1/5$	41.8	42	44.8	44.6	44.6	42.2
$k_5 = V_1/5$	42.8	45.4	49.4	46.2	49	45.2
R_i	2.2	4.8	14	8.8	14.8	5

Note. R_i represents the range of values under various factor conditions.

followed by the drop height, the slider thickness, the slider length, the slider width, and the still water depth.

3.3. Prediction of the Maximum Wave Height

3.3.1. Definition of the Maximum Wave Height. Figure 5 shows the four distinct phases defined by Huber and Hager [43]. Phase 1 is when the landslide begins moving, accelerates, and then falls into the water. Phase 2 is the underwater movement of the landslide, which is also referred to as the generation area or the splash zone in the case of a subaerial landslide. During phase 2, the energy of the landslide is transferred to the water [33, 34]. Phase 3 refers to the propagation of the water waves. Phase 4 is when the impulse wave reaches the water body boundaries and runs up or over the top of the dams, which eventually poses a great threat to human lives and property.

Figure 6 depicts a typical waveform signal record from the experiments. As is defined by Panizzo et al. [1] and Walder et al. [33], a standard zero-crossing analysis was carried out

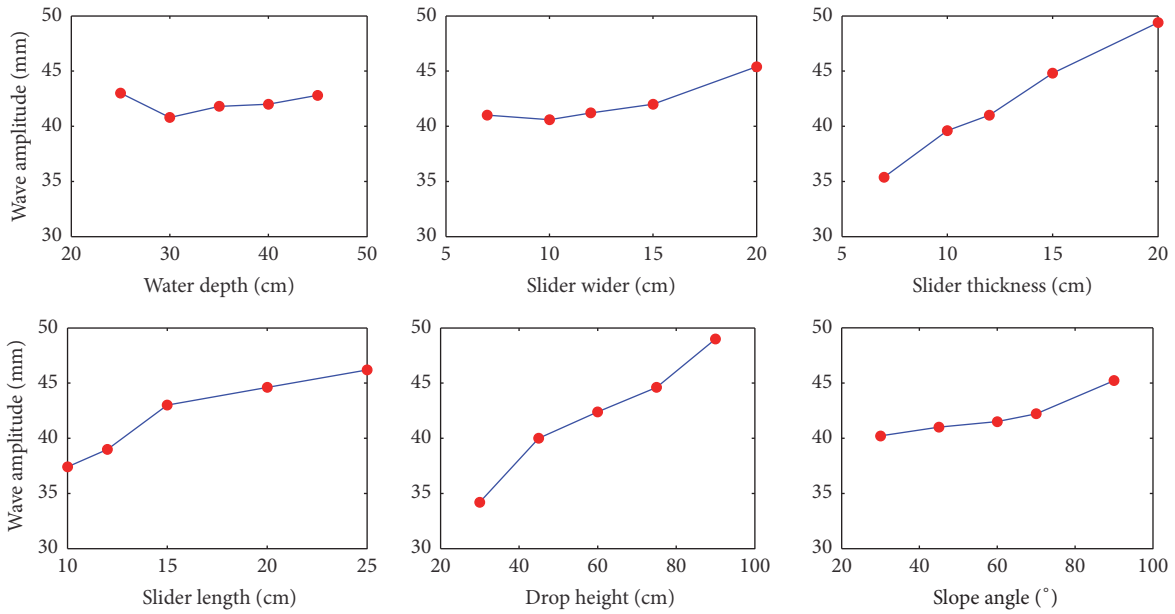

Figure 4: Relationship between the wave height and all of the influencing factors.

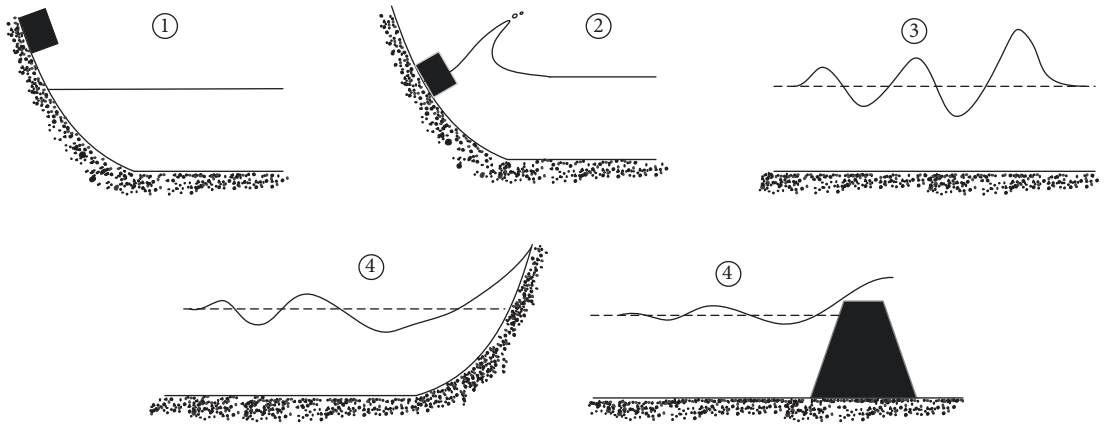

Figure 5: Main phases of landslides-generated impulse waves.

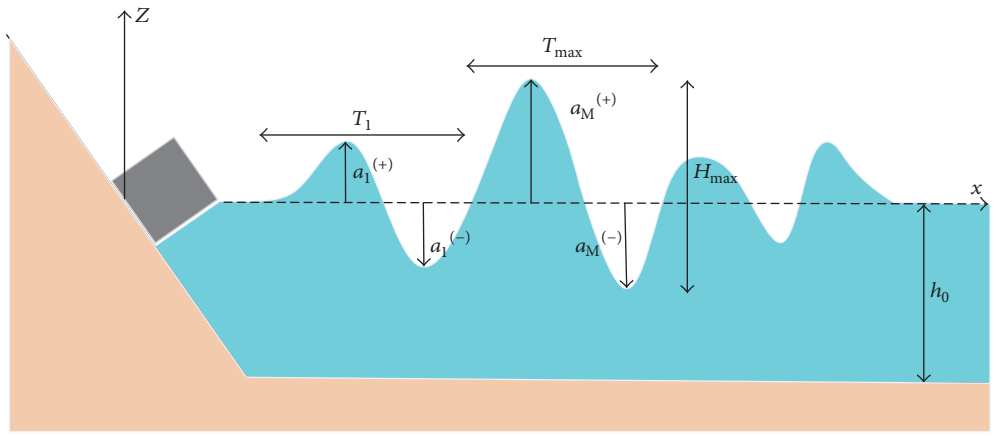

Figure 6: Sketch of an impulse wave and the primary wave parameters.

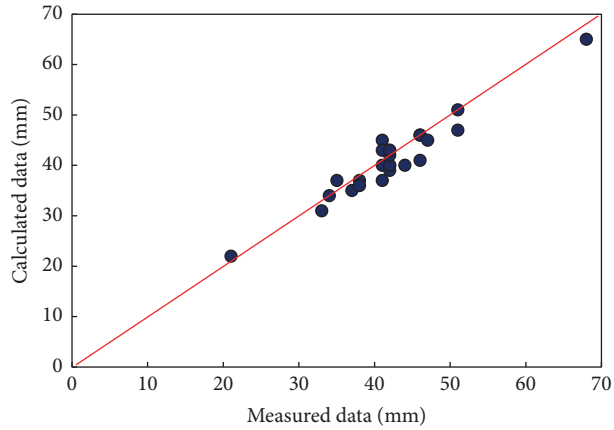

Figure 7: Comparison between measured values and predicted values.

Table 4: Relationship between H_r/h_0 and x/h_0 for each experiment.

	H_{max}/d	$H_r/d = ke^{-m(x/d)}$		
		k	m	R^2
T1	0.084	0.081	0.050	0.913
T2	0.119	0.120	0.049	0.955
T3	0.155	0.146	0.045	0.940
T4	0.181	0.166	0.043	0.915
T5	0.260	0.238	0.042	0.950
T6	0.140	0.126	0.049	0.934
T7	0.153	0.135	0.052	0.882
T8	0.127	0.127	0.058	0.960
T9	0.130	0.118	0.052	0.870
T10	0.117	0.103	0.049	0.851
T11	0.113	0.111	0.040	0.950
T12	0.120	0.109	0.054	0.933
T13	0.131	0.128	0.050	0.938
T14	0.120	0.125	0.056	0.948
T15	0.106	0.093	0.039	0.968
T16	0.118	0.109	0.043	0.909
T17	0.103	0.100	0.047	0.908
T18	0.095	0.100	0.056	0.909
T19	0.105	0.101	0.062	0.952
T20	0.103	0.110	0.048	0.865
T21	0.113	0.113	0.064	0.888
T22	0.091	0.080	0.043	0.884
T23	0.093	0.087	0.049	0.869
T24	0.076	0.065	0.055	0.900
T25	0.102	0.103	0.054	0.858

to define the maximum wave amplitude (a_M). The wave amplitude reported here is the elevation of the water surface relative to the datum (still water) within the zero-crossing wave. The maximum impulse wave height is the difference between the absolute maximum and the absolute minimum values within the maximum zero-crossing wave. The related wave period (T_{max}), which is important to wave propagation, and the first wave of the generated transient train ($a_1^{(+)}$, $a_1^{(-)}$, and T_1) were also characterized. The video images were analyzed frame by frame, and, then, the captured images were printed to measure the maximum height of the wave. The error of the measured maximum wave height is caused by the image resolution (0.4 mm per pixel) and blurring of the image (from a limited exposure time). We estimate that the error is typically within the range of 1 to 2 mm. The wavelet analysis method was used to compute the zero cross section of the wave records. Based on the work of Panizzo et al. [44], wavelet analysis was used to make a part of the wave field propagate away from the impact point, thus reducing the effect of the reflected wave on the recorded wave signal.

3.3.2. Equation for the Maximum Wave Height. The data recorded by the wave gauges was used to derive the prediction equations for the impulse wave's characteristics. Based on dimensional analysis, the relationship between the wave height and the four dimensionless parameters is as follows:

$$\frac{H_{max}}{d} = f\left(\frac{v}{\sqrt{gd}}, \frac{w}{d}, \frac{V_s}{bd^2}, \frac{T_s}{A_w{}^*}, \alpha\right), \quad (11)$$

where the nondimensional parameter $A_w{}^* = bs/d^2$ summarizes the landslide geometry. We can obtain an empirical equation through multiple linear regression analysis, and the relationship between the maximum wave height and the five dimensionless parameters can be expressed by (11) as follows:

$$\frac{H_{max}}{d} = 0.145F^{0.672}B^{0.09}V^{0.217}\left(\frac{T_s}{A_w{}^*}\right)^{-0.045}\alpha^{0.038}. \quad (12)$$

Figure 7 compare the calculated and measured wave heights of each experiment. It can be seen from Figure 7 that the empirical equation is basically consistent with the experimental data for all of the different experimental conditions.

In actual landslides, T_s is a dependent variable and must be calculated. Panizzo et al. [1] developed an empirical equation for estimating T_s:

$$T_s = 0.43V^{-0.27}F^{-0.66}(\sin\alpha)^{-1.32}. \quad (13)$$

Equation (13) correlates well with our experimental measurements and is therefore useful in determining T_s.

3.4. Equation for Wave Height Attenuation. The attenuation calculation of the landslide surge is based on the basic continuity equation and the motion equation for unsteady flow in an open channel (Li [45]):

$$\begin{aligned} T\frac{\partial h}{\partial t} + u\frac{\partial h}{\partial x} + A\frac{\partial u}{\partial x} + bu - q = 0, \\ g\frac{\partial h}{\partial x} + \frac{\partial u}{\partial t} + u\frac{\partial u}{\partial x} + g\left(j - i\right) = 0, \end{aligned} \tag{14}$$

where $T(h, x)$ is the water surface width; $A(h, x)$ is the section area; $u(x, t)$ is the flow velocity; $h(x, t)$ is the water depth; j is the energy slope; i is the bed slope; and q is the increased flow per unit length. We use the hydrodynamic perturbation method to expand the continuity equation and the motion equation into polynomials. If we assume that the increased flow per unit length (q) is zero and that the friction slope (j) in the fluid is proportional to the local velocity, then (14) can be simplified as follows:

$$\begin{aligned} T\frac{\partial h}{\partial t} + uT\frac{\partial h}{\partial x} + A\frac{\partial u}{\partial x} + bu = 0, \\ g\frac{\partial h}{\partial x} + \frac{\partial u}{\partial t} + u\frac{\partial u}{\partial x} + g\left(ku - i\right) = 0. \end{aligned} \tag{15}$$

In order to solve (15), we can use the hydrodynamic perturbation method to linearize the equation. We assume that $\overline{h}$ is the representative water depth, δ is the wave height, and $\varepsilon = \delta/\overline{h}$. In the perturbation method, the solutions of u and h can often be expressed as follows:

$$\begin{aligned} u\left(x, t\right) &= u_0\left(x, t\right) + \varepsilon u_1\left(x, t\right) + \varepsilon^2 u_2\left(x, t\right) + \cdots, \\ h\left(x, t\right) &= h_0\left(x, t\right) + \varepsilon h_1\left(x, t\right) + \varepsilon^2 h_2\left(x, t\right) + \cdots, \end{aligned} \tag{16}$$

where the values of $u_0, u_1, \ldots, h_0, h_1, \ldots$ need to be determined and sometimes need other forms of expansion as noted by Kevorkian and Cole [46]. By substituting (16) into (15), we obtained the following equations:

$$\begin{aligned} &\left(\varepsilon u_1 + \cdots\right)\frac{\partial}{\partial x}\left(\varepsilon u_1 + \cdots\right) + \frac{\partial}{\partial t}\left(\varepsilon u_1 + \cdots\right) \\ &\quad + g\frac{\partial}{\partial x}\left(h_0 + \varepsilon h_1 + \cdots\right) + g\left(\varepsilon k u_1 + \cdots - i\right) = 0, \\ &\left(A_0 + \cdots\right)\frac{\partial}{\partial x}\left(\varepsilon u_1 + \cdots\right) \\ &\quad + \left(\varepsilon u_1 + \cdots\right)\left(T_0 + \cdots\right)\frac{\partial}{\partial x}\left(h_0 + \cdots\right) \\ &\quad + \left(T_0 + \cdots\right)\frac{\partial}{\partial t}\left(h_0 + \varepsilon h_1 + \cdots\right) \\ &\quad + \left(\varepsilon u_1 + \cdots\right)\left(b_0 + \cdots\right) = 0. \end{aligned} \tag{17}$$

By simplifying (17) to the idempotent ε, we can obtain the following equations:

$$\begin{aligned} \varepsilon\left(T_0\frac{\partial h_1}{\partial t} + u_1\frac{dA_0}{dx} + A_0\frac{\partial u_1}{\partial x} + T_1\frac{\partial h_0}{\partial t}\right) + \cdots = 0, \\ g\left(\frac{\partial h_0}{\partial x} - i\right) + \varepsilon\left(\frac{\partial u_1}{\partial t} + g\frac{\partial h_1}{\partial x} + gku_1\right) + \cdots = 0. \end{aligned} \tag{18}$$

Since (18) are assumed to be valid for any small value of ε, they are effective for each derivative of ε, so the equations for the zero order are as follows:

$$\begin{aligned} T_0\frac{\partial h_0}{\partial t} = 0, \\ g\frac{\partial h_0}{\partial x} - i = 0, \end{aligned} \tag{19}$$

where u_s represents the flow velocity (εu_1) and h_s represents the displacement (εh_1). Thus, the equations for the first order are as follows:

$$\begin{aligned} T_0\frac{\partial h_s}{\partial t} + u_s\frac{dA_0}{dx} + A_0\frac{\partial u_s}{\partial x} = 0, \\ \frac{\partial u_s}{\partial t} + g\frac{\partial h_s}{\partial x} + gku_s = 0. \end{aligned} \tag{20}$$

Using (20) to eliminate u, we obtain the following:

$$T_0\frac{\partial^2 h_s}{\partial t^2} + gkT_0\frac{\partial h_s}{\partial t} = A_0 g\frac{\partial^2 h_s}{\partial x^2} + g\frac{dA_0}{dx}\frac{\partial h_s}{\partial x}. \tag{21}$$

For rectangular or approximately rectangular channels, $dA_0/dx = 0$, so Equation (21) can be written as follows:

$$T_0\frac{\partial^2 h_s}{\partial t^2} + gkT_0\frac{\partial h_s}{\partial t} = A_0 g\frac{\partial^2 h_s}{\partial x^2}. \tag{22}$$

After the landslide occurs, the surface of the water rises, then falls rapidly, and soon develops an oscillation with a small height. It can be assumed that the descent process obeys an exponential distribution. Therefore, we assume $h_s(x, t) = f(x)e^{-at}$, and (22) can be changed to

$$T_0 a^2 f\left(x\right)e^{-at} - gkT_0 af\left(x\right)e^{-at} = A_0 gf''\left(x\right)e^{-at}. \tag{23}$$

If $k_1 = (T_0 a^2 - gkT_0 a)/A_0 g$, then $f''(x) = k_1 f(x)$, and we obtain the following equation:

$$f\left(x\right) = C_1 e^{\sqrt{k_1}x} + C_2 e^{\sqrt{k_2}x}. \tag{24}$$

Applying the boundary condition $f(0) = h_j$, $\lim_{x\to\infty} f(x) = 0$, we get $C_1 = 0$, $C_2 = h_j$; therefore,

$$h_s\left(x, t\right) = h_j e^{-\sqrt{k_1}x - at} = ke^{-mx}. \tag{25}$$

Next, we use the experimental data to verify and fit the equation. According to the data recorded by each wave instrument, the free surface height of the water body at different times can be obtained. Figure 8 shows the variation

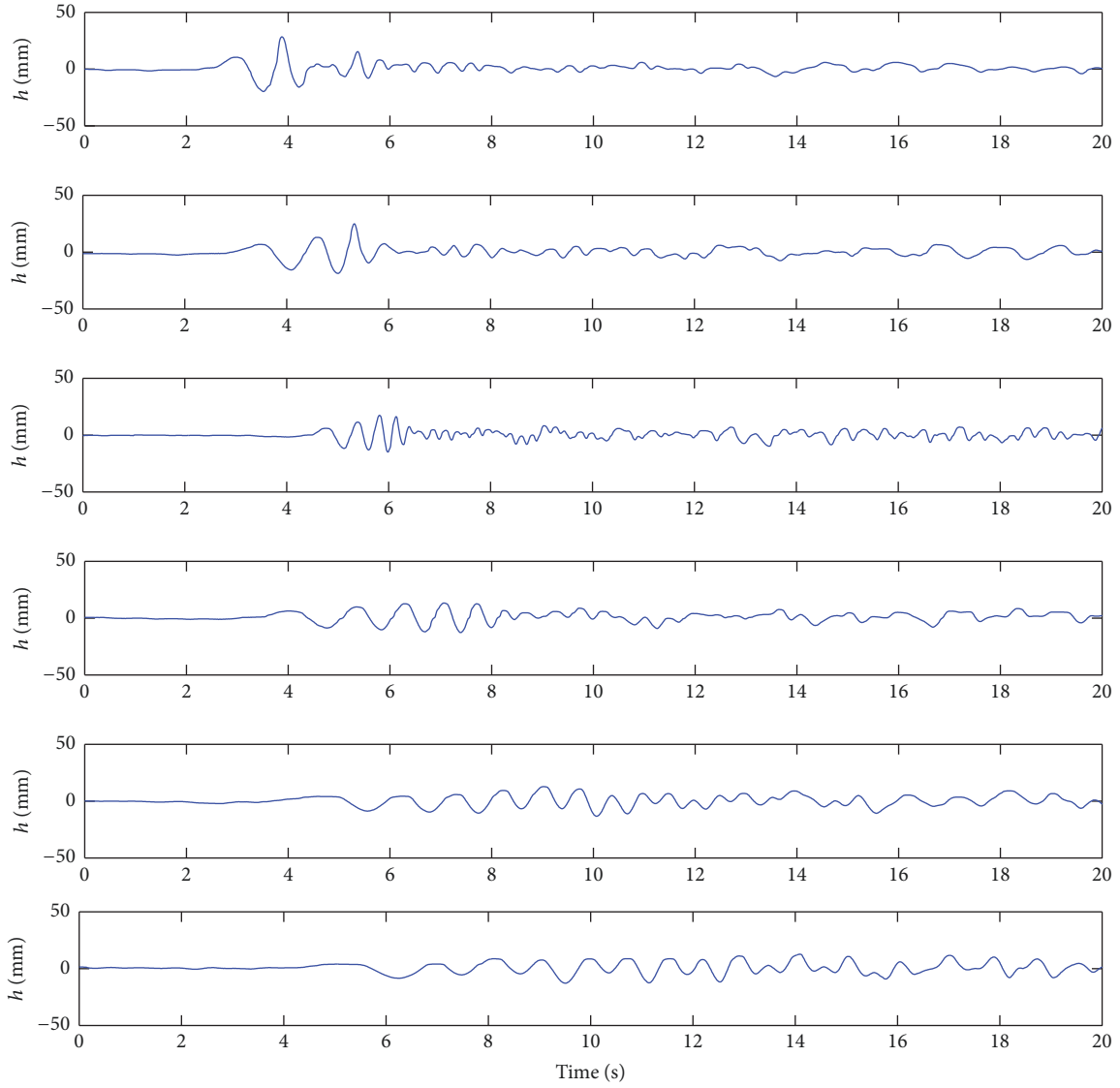

Figure 8: Variation in height of the surge with time for different points in the same experiment.

in wave height with time for different positions in the same experiment.

The study of the factors affecting the attenuation of the landslide induced surge was carried out based on the wave height data of the 6 wave instruments. At different water depths, the relative distances of the six wave instruments along the cross section of the flume are shown in Figure 9.

H_r/d can be roughly fitted by an exponential power function

$$\frac{H_r}{d} = ke^{-m(x/d)}. \tag{26}$$

H_r is the height of the waves propagating along the flume. Table 4 lists the parameters for each experiment with $R^2 \approx 1$ for almost all cases.

We find that, in each experiment, the values of k and $H_{\max}/d$ are very close; thus, the equation for the propagation of waves along the propagating path can be expressed as follows:

$$\frac{H_r}{d} = \frac{H_{\max}}{d} e^{-0.05(x/d)}. \tag{27}$$

Equation (27) is still able to effectively describe the attenuation of the impulse wave's height, with a maximum error value of ≤15%.

4. A Case Study

The Zipingpu reservoir is located on the upper reaches of the Ming River in Maxi Town, which is about 30 km from Wenchuan county, Sichuan province, China. The reservoir was completed in 2006, and its water storage capacity is 11 billion cubic meters. The height of the dam is 156 meters, and the full-pool level altitude is 817 m.

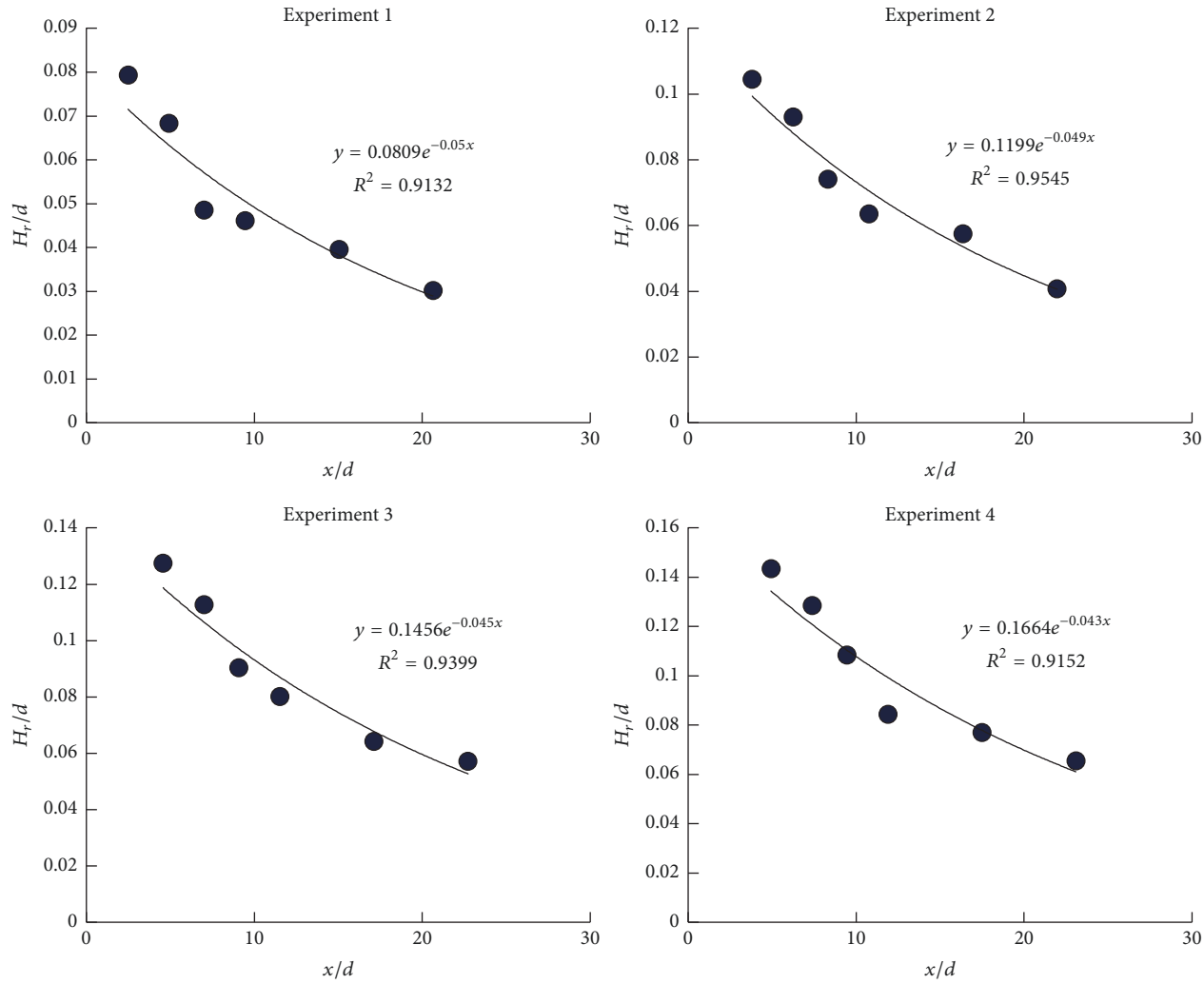

Figure 9: Maximum wave heights versus the relative propagation distance.

The Zipingpu landslide was a typical high-velocity landslide that occurred 15.5 km away from the earthquake epicenter. It occurred at 14:29 on 12 May 2008, about half a minute after the Wenchuan earthquake. A 25 m high huge impulse wave was observed to spread rapidly downstream. This surge killed more than 70 fishermen and destroyed more than 10 fishing boats along the shore. The Zipingpu landslide area is an irregular quadrilateral plane 180 m × 100 m × 25 m with a total volume of 4.5×10^5 m^3. The vertical distance from the landslide center to the water surface is 900 m, and the average sliding surface angle is 48°.

Assuming that the landslide entered the reservoir as one large mass, we can use (28), as recommended by the American Society of Civil Engineers [42], to calculate the entry velocity of the landslide:

$$v_s = \sqrt{2gh\left[(1 - \cot\alpha \tan\varphi) - \frac{cL}{mg\sin\alpha}\right]}, \quad (28)$$

where α is the sliding surface angle; c and φ are shear strength parameters of sliding surface; H is the vertical distance from the landslide's center to the water's surface; m is the mass of the slider; and L is the length of the slider and the sliding surface. The calculated velocity of the landslide is 66.31 m/s. Using this velocity, the calculated maximum impulse wave height is 26.6 m.

We use the empirical equation proposed by previous researchers to calculate 26.6 m for the case study, after which the calculated values are compared with the results of this paper and the measured data. The results are presented in Table 5.

As can be seen form Table 5, the calculated result is very close to the result of the eye-witness observations and the calculations of other researchers. In addition, the proposed equation takes into account parameters such as the landslide's shape and the slope of the sliding surface, both of which are important to the formation of the impulse wave. Thus, the equations proposed in this paper are more suitable for practical cases.

Table 5: Comparison of the presented forecasting equations.

Method of calculation	Formula	Wave height (m)
Observed value	-	25
Equation in this paper	-	26.6
Cui and Zhu [42]	$0.108F^{1.669}V^{0.045}S^{0.36}\alpha_0{}^{-1.636}$	23.1
Noda [8]	$1.32F$	24.3
Walder et al. [33]	$1.32(\tau/M)^{-0.68}$, with $\tau = 4.5\mathrm{L}^{0.5}$	22.6
Fritz et al. [15]	$0.25F^{1.4}S^{0.8}$	19.6
Panizzo et al. [40]	$0.102\sum^{0.572}F^{0.297}R^{-0.44}(\sin 4)^{-0.286}\exp(0.6\cos\theta)$	16.4

5. Conclusions

The characteristics of the maximum impulse wave's height and its attenuation were experimentally investigated using the orthogonal method. The experimental results were employed to develop an empirical equation to predict the maximum wave height for different landslide sizes and volumes. The following conclusions were generated.

(1) It is possible to reduce the number of experiments and shorten the experimental period by using the orthogonal design. The reasonable mathematical statistical analysis of the experimental data in the orthogonal table can reveal the regularity and internal relationships between the index and the factors and can be used to guide the practice.

(2) The results of the orthogonal experiments indicate that the initial drop height and slider thickness are the main factors affecting the wave height, then the slider length, slider width, sliding slope, and still water depth.

(3) The relationship between the wave height and the four dimensionless parameters can be expressed as follows:

$$\frac{H_{\max}}{d} = 0.145F^{0.672}B^{0.09}V^{0.217}\left(\frac{T_s}{A_W{}^*}\right)^{-0.045}\alpha^{0.038}. \quad (29)$$

(4) The hydrodynamic perturbation method was used to expand the continuity and motion equations into polynomials; it is concluded that the wave decay process exhibits an exponential form, and, by separating the variables, the attenuation law of the landslide wave was obtained.

Appendix

Orthogonal design is a method of arranging and analyzing an experiment. It can scientifically arrange the experiment using a special design tool called an "orthogonal table" and carry out statistical analysis of the corresponding experimental results. It can also obtain the maximum possible amount of useful information from as few experiments as possible. After which, it can perform an effective statistical analysis of the obtained information and make it possible for reliable inference to be made. In addition, further analysis can be done to obtain more useful information than could be obtained solely from the experimental results. This method has proven very useful and reliable, so it is widely used.

In a comprehensive experiment, when the number of factors and levels increases, the number of experiments required will rapidly increase as an exponential power function. For example, for an experiment that contains 6 factors with 5 levels each, the comprehensive experiment requires $5^6 = 15625$ combinations, which is almost impossible to achieve, but orthogonal design can help us achieve the same goal using fewer experiments. In the experimental arrangement, for each factor a few levels are selected within the scope of the study, which is similar to creating a grid in the optimal area. If every point on the grid is experimented, it is a comprehensive experiment. For example, 3 factors in the optimal area can be expressed by a cube (Figure 10(a)), and the 3 factors each have 3 levels, which divides the cube into 27 lattice points. A comprehensive experiment would require experimenting with 27 grid points. The experimental scheme for this hypothetical experiment is shown in Table 6.

The number of comprehensive experiments for 3 factors with 3 levels each is $3^3 = 27$, 4 factors with 3 levels each is $3^4 = 81$, 5 factors with 3 levels each is $3^5 = 243$, and so on. It is difficult to conduct all of the experiments required by designs with multiple factors and multiple levels. An orthogonal experiment can select a representative part of the comprehensive experiment points from the optimal area to carry out the experiment. In Figure 10(a), the 9 spots marked with experimental numbers are the experimental points selected from the 27 experimental points using orthogonal table $L_9(3^4)$, which refers to the designs that are both orthogonal and balanced, and, hence, are optimal. Figure 10(b) explains the meaning of the symbols and numbers in the orthogonal table.

From Table 7, we can see that, in the three groups of experiments, three different levels of factor B and C appeared once in each group. The difference is that factor A's level remains the same in the same experiment group and varies between groups. Thus, the average value of the experimental results of the three different levels of A ($\overline{k}_{1A}$, $\overline{k}_{2A}$, and $\overline{k}_{3A}$) is not related to the level of factors B and C, so they mainly reflect the difference between A_1, A_2, and A_3. It can be considered that the values of $\overline{k}_{1A}$, $\overline{k}_{2A}$, and $\overline{k}_{3A}$ reflect the advantages and disadvantages of factor levels A_1, A_2, and A_3. This is why the optimal level of factor A is determined by the values of $\overline{k}_{1A}$, $\overline{k}_{2A}$, and $\overline{k}_{3A}$ when choosing the optimal level combination scheme. This indicates that the orthogonal experimental design method can reasonably be used to compare the different levels of

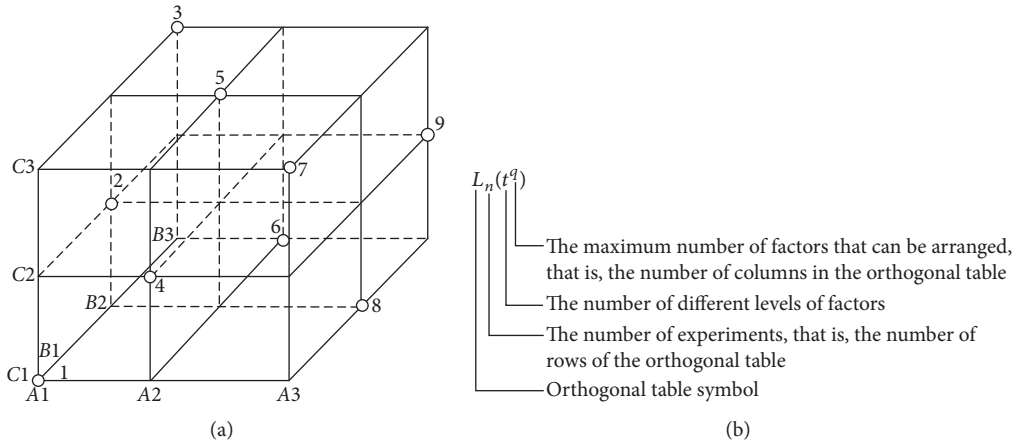

Figure 10: Graphic illustrations, symbols, and meanings of the orthogonal experiment design.

Table 6: 3 comprehensive experimental schemes for factors with 3 levels each.

		C_1	C_2	C_3
A_1	B_1	$A_1B_1C_1$	$A_1B_1C_2$	$A_1B_1C_3$
	B_2	$A_1B_2C_1$	$A_1B_2C_2$	$A_1B_2C_3$
	B_3	$A_1B_3C_1$	$A_1B_3C_2$	$A_1B_3C_3$
A_2	B_1	$A_2B_1C_1$	$A_2B_1C_2$	$A_2B_1C_3$
	B_2	$A_2B_2C_1$	$A_2B_2C_2$	$A_2B_2C_3$
	B_3	$A_2B_3C_1$	$A_2B_3C_2$	$A_2B_3C_3$
A_3	B_1	$A_3B_1C_1$	$A_3B_1C_2$	$A_3B_1C_3$
	B_2	$A_3B_2C_1$	$A_3B_2C_2$	$A_3B_2C_3$
	B_3	$A_3B_3C_1$	$A_3B_3C_2$	$A_3B_3C_3$

Table 7: Orthogonal tables arranged at different levels according to factor A.

Experiment group number	Experiment number	Factor		
		A	B	C
I	1	1	1	1
	2	1	2	2
	3	1	3	3
II	4	2	1	2
	5	2	2	3
	6	2	3	1
III	7	3	1	3
	8	3	2	1
	9	3	3	2

factor A when the levels of factors B and C are changing. This property is called the "comprehensive comparability" or "symmetrical comparability." This is because the orthogonal table used to arrange the experiment has "equilibrium dispersion" and "symmetrical comparability" characteristics. Therefore, the collection of comprehensive information is still sufficient despite a large reduction in the number of experiments.

Conflicts of Interest

The authors declare that they have no conflicts of interest.

Acknowledgments

This study was financially supported by the Natural Science Foundation of China under Contract no. 41571004, Scientific

and Technological Research and Development Plan of China Railway Corporation (no. 2015G002-N), and Natural Science Foundation of China (no. 41172321). The authors express their gratitude to these foundations.

References

[1] A. Panizzo, P. De Girolamo, M. Di Risio, A. Maistri, and A. Petaccia, "Great landslide events in Italian artificial reservoirs," *Natural Hazards and Earth System Sciences*, vol. 5, no. 5, pp. 733–740, 2005.

[2] C. E. Synolakis, J.-P. Bardet, J. C. Borrero et al., "The slump origin of the 1998 papua new guinea tsunami," in *Proceedings of the royal society of london A: Mathematical, physical and engineering sciences*, vol. 458, pp. 763–789.

[3] M. H and Fritz., "Lituya Bay case rockslide impact and wave run-up," *Science of Tsunami Hazards*, vol. 19, no. 1, pp. 3–22, 2001.

[4] C. B. Harbitz, G. Pedersen, and B. Gjevik, "Numerical simulations of large water waves due to landslides," *Journal of Hydraulic Engineering*, vol. 119, no. 12, pp. 1325–1342, 1993.

[5] D. J. Miller, *Giant waves in lituya bay*, US Government Printing Office, Alaska, Washington DC, USA, 1960.

[6] A. Huber, "Quantifying impulse wave effects in reservoirs," in *Transactions of The International Congress on Large Dams*, vol. 3, pp. 563–582, 1997.

[7] E. H. Kennard, "Generation of surface waves by a moving partition," *Quarterly of Applied Mathematics*, vol. 7, no. 3, pp. 303–312, 1949.

[8] E. Noda, "Water waves generated by landslides," *Journal of the Waterways, Harbors and Coastal Engineering Division*, vol. 96, no. 4, pp. 835–855, 1970.

[9] J. Pan, *Analysis of Stability against Sliding of Buildings and Landslides*, China Water Conservancy Press, Beijing, China, 1980.

[10] P. Lynett and P. L.-F. Liu, "A numerical study of the run-up generated by three-dimensional landslides," *Journal of Geophysical Research: Oceans*, vol. 110, no. 3, pp. 1–16, 2005.

[11] A. Romano, G. Bellotti, and M. Di Risio, "Wavenumber-frequency analysis of the landslide-generated tsunamis at a conical island," *Coastal Engineering Journal*, vol. 81, pp. 32–43, 2013.

[12] E. Pelinovsky, *Analytical models of tsunami generation by submarine landslides*, Submarine landslides and tsunamis, Springer, Netherlands, 2003.

[13] M. Quecedo, M. Pastor, and M. I. Herreros, "Numerical modelling of impulse wave generated by fast landslides," *International Journal for Numerical Methods in Engineering*, vol. 59, no. 12, pp. 1633–1656, 2004.

[14] B. Ataie-Ashtiani and S. Malek-Mohammadi, "Mapping impulsive waves due to sub-aerial landslides into a dam reservoir: a case study of shafa-roud dam," *Dam Engineering*, vol. 18, no. 4, p. 243, 2008.

[15] H. M. Fritz, W. H. Hager, and H.-E. Minor, "Near field characteristics of landslide generated impulse waves," *Journal of Waterway, Port, Coastal, and Ocean Engineering*, vol. 130, no. 6, pp. 287–302, 2004.

[16] M. Di Risio and P. Sammarco, "Analytical modeling of landslide-generated waves," *Journal of Waterway, Port, Coastal, and Ocean Engineering*, vol. 134, no. 1, pp. 53–60, 2008.

[17] R. P. Mulligan and W. A. Take, "On the transfer of momentum from a granular landslide to a water wave," *Coastal Engineering Journal*, vol. 125, pp. 16–22, 2017.

[18] Y.-P. Yin, B. Huang, X. Chen, G. Liu, and S. Wang, "Numerical analysis on wave generated by the qianjiangping landslide in three gorges reservoir, China," *Landslides*, vol. 12, no. 2, pp. 355–364, 2015.

[19] S. Bosa and M. Petti, "Shallow water numerical model of the wave generated by the Vajont landslide," *Environmental Modeling and Software*, vol. 26, no. 4, pp. 406–418, 2011.

[20] D. Risio, M. Paolo De Girolamo, and G. Mario Beltrami, "Forecasting landslide generated tsunamis: a review," *The tsunami threat-research and technology*, 2011, Intech.

[21] H. M. Fritz et al., "Laser Techniques for Fluid Mechanics," J. R. Adrian, Ed., pp. 305–520, Springer, New York, NY, USA, 2002.

[22] V. Heller and W. H. Hager, "Impulse product parameter in landslide generated impulse waves," *Journal of Waterway, Port, Coastal, and Ocean Engineering*, vol. 136, no. 3, Article ID 001003QWW, pp. 145–155, 2010.

[23] J. S. Walder, O. E. Sorensen, and P. Watts, Water waves generated by subaerial mass flows, AGU Fall Meeting Abstracts. 2001.

[24] H. M. Fritz, W. H. Hager, and H.-E. Minor, "Landslide generated impulse waves. 1. Instantaneous flow fields," *Experiments in Fluids*, vol. 35, no. 6, pp. 505–519, 2003.

[25] V. Heller, W. H. Hager, and H.-E. Minor, "Scale effects in subaerial landslide generated impulse waves," *Experiments in Fluids*, vol. 44, no. 5, pp. 691–703, 2008.

[26] G. S. Miller, W. Andy Take, R. P. Mulligan, and S. McDougall, "Tsunamis generated by long and thin granular landslides in a large flume," *Journal of Geophysical Research: Oceans*, vol. 122, no. 1, pp. 653–668, 2017.

[27] H. M. Fritz, W. H. Hager, and H.-E. Minor, "Landslide generated impulse waves. 2. Hydrodynamic impact craters," *Experiments in Fluids*, vol. 35, no. 6, pp. 520–532, 2003.

[28] F. Liu, T. R. Wu, F. Raichlen, C. E. Synolakis, and J. C Borrero, "Runup and rundown generated by three-dimensional sliding masses," *Journal of fluid Mechanics*, vol. 536, pp. 107–144, 2005.

[29] F. Enet and T. Grilli, "Experimental study of tsunami generation by three-dimensional rigid underwater landslides," *Journal of Waterway, Port, Coastal, and Ocean Engineering*, vol. 133, no. 6, pp. 442–454, 2007.

[30] G. Zitti, C. Ancey, M. Postacchini, and M. Brocchini, "Impulse waves generated by snow avalanches: Momentum and energy transfer to a water body," *Journal of Geophysical Research: Earth Surface*, vol. 121, no. 12, pp. 2399–2423, 2016.

[31] P. Watts, *Water waves generated by underwater landslides [Msc. Thesis]*, California Institute of Technology, 1997.

[32] P. Watts, "Wavemaker curves for tsunamis generated by underwater landslides," *Journal of Waterway, Port, Coastal, and Ocean Engineering*, vol. 124, no. 3, pp. 127–136, 1998.

[33] J. S. Walder, P. Watts, O. E. Sorensen, and K. Janssen, "Tsunamis generated by subaerial mass flows," *Journal of Geophysical Research: Solid Earth*, vol. 108, no. 5, 2003.

[34] P. Sammarco and M. Di Risio, "Sul generatore di Scott Russell, paper presented at IDRA 2004," in *Proceedings of the Conference of Idraulica e Costruzioni Idrauliche*, Trento, Italy, 2004.

[35] V. Heller and J. Spinneken, "On the effect of the water body geometry on landslide-tsunamis: Physical insight from laboratory tests and 2D to 3D wave parameter transformation," *Coastal Engineering Journal*, vol. 104, pp. 113–134, 2015.

[36] V. Heller, M. Bruggemann, J. Spinneken, and B. D. Rogers, "Composite modelling of subaerial landslide-tsunamis in different water body geometries and novel insight into slide and wave kinematics," *Coastal Engineering Journal*, vol. 109, pp. 20–41, 2016.

[37] M. Di Risio, G. Bellotti, A. Panizzo, and P. De Girolamo, "Three-dimensional experiments on landslide generated waves at a sloping coast," *Coastal Engineering Journal*, vol. 56, no. 5-6, pp. 659–671, 2009.

[38] M. Di Risio, P. De Girolamo, G. Bellotti et al., "Landslide-generated tsunamis runup at the coast of a conical island: New physical model experiments," *Journal of Geophysical Research: Oceans*, vol. 114, no. 1, Article ID C01009, 2009.

[39] A. Romano, M. Di Risio, G. Bellotti, M. G. Molfetta, L. Damiani, and P. De Girolamo, "Tsunamis generated by landslides at the coast of conical islands: experimental benchmark dataset for mathematical model validation," *Landslides* , vol. 13, no. 6, pp. 1379–1393, 2016.

[40] A. Panizzo, P. De Girolamo, and A. Petaccia, "Forecasting impulse waves generated by subaerial landslides," *Journal of Geophysical Research: Oceans*, vol. 110, no. 12, Article ID C12025, pp. 1–23, 2005.

[41] A. V. Geramita and J. Seberry, *Orthogonal Designs: Quadratic Forms and Hadamard Matrices*, vol. 45 of *Lecture Notes in Pure and Applied Mathematics*, Marcel Dekker, Inc., New York, NY, USA, 1979.

[42] P. Cui and X. Zhu, "Surge generation in reservoirs by landslides triggered by the wenchuan earthquake," *Journal of Earthquake and Tsunami*, vol. 5, no. 5, pp. 461–474, 2011.

[43] A. Huber and W. H. Hager, "Forecasting impulse waves in reservoirs," in *Transactions of The International Congress on Large Dams*, vol. 1, pp. 993–1006, 1997.

[44] A. Panizzo, G. Bellotti, and P. De Girolamo, "Application of wavelet transform analysis to landslide generated waves," *Coastal Engineering Journal*, vol. 44, no. 4, pp. 321–338, 2002.

[45] W. H. Li, *Differential equations of hydraulic transients, dispersion, and groundwater flow: mathematical methods in water resources*, Prentice Hall, 1972.

[46] J. D. Kevorkian and J. D. Cole, *Perturbation Methods in Applied Mathematics*, vol. 34, Springer Science Business Media, 2013.